RSC Advances

ROYAL SOCIETY OF CHEMISTRY

www.rsc.org/advances

Journal Name

ARTICLE

A simple and room temperature sol-gel process in fabrication of cobalt nanoparticles as effective catalyst for carbon nanotube growth

Received 00th January 20xx,
Accepted 00th January 20xx

DOI: 10.1039/x0xx00000x

www.rsc.org/

Nor Najihah Zulkapli, Mohd Asyadi Azam*, Nik Mohamad Azren Mohd Zubir, Nur Azura Ithnin and Mohd Warikh Abd Rashid

Cobalt catalyst thin film was prepared on silicon wafers by spin coating process. A detailed structural characteristics of cobalt films/particles and synthesized carbon nanotubes were studied using X-ray analyses, high resolution electron microscopies, and Raman spectroscopy. The thickness of the catalyst thin films can be controlled by controlling the spin coating parameter, and the thickness of the films can be reduced by increasing the spin speed. Cobalt catalyst particles can be achieved by post-heat treatment within the range of 450–600 °C. However, increasing post-heat treatment temperature may lead to larger particle formation. The optimum thin film thickness and particle size was 12.1 nm at 8000 rpm and 10.6 nm at 450 °C, accordingly. The study also demonstrated that single-walled carbon nanotubes could be grown from cobalt catalyst particles via catalytic chemical vapor deposition of ethanol.

Introduction

The development in nanotechnology has led to the growth of carbon nanotubes (CNTs). This development leads to the large potential of CNTs in electric and electrical industries, such as photovoltaic, sensors, semiconductor devices, displays, and conductor [1-2]. Catalyst nanoparticles are essential for growing CNT. These catalyst nanoparticles can be obtained from thin film after heat treatment process. However, controlling catalyst formation can improve CNT growth. Thin film consists of a thin layer of resistor material deposited on the surface of a substrate, followed by a thin layer of metal. Thin film is formed mostly by deposition, either by physical or chemical method [3-4]. Transition metals, such as iron, cobalt, and nickel, are reported to be the most effective catalysts to grow CNT because of their high carbon solubility at high temperature and high diffusion rate [5]. Among these three potential transition metals for CNT growth, Co is selected as catalyst because it can produce good quality CNT and it is the most reactive catalyst for ethanol-based chemical vapor deposition (CVD) system [6-7].

In CNT production, physical vapor deposition (PVD) method is widely used to produce thin film, which is a layer that contains the catalyst nanoparticles. These catalysts are important in CNT growth by alcohol catalytic CVD (ACCVD). PVD is commonly used for the industrial scale of catalyst film production; this technique is suitable to obtain uniform thin film and control its thickness. However, the ratio of deposited material after deposition is less than 10% of the source material. The accumulated material is then scraped off using photolithographic method. Thus, about 99% of the expensive high technology material is wasted; moreover, the coating rate is slow. The machine needs high vacuum system and large cooling system to evacuate the air inside the chamber and cool down the system during the deposition process, respectively. Therefore, the solution process, specifically spin coating, is a promising technique to produce uniform, ultrathin film with thickness of a nanometer [8]. Furthermore, solution process technique has been given high attention because of its simple deposition procedure, easy control of chemical components, and low cost preparation to obtain high quality thin films [9].

ACCVD is the most assuring technique in CNT growth because of its wide substrate selectivity, good economic value, and high catalytic reaction [10–12]. The CNT grown from this technique has high potential in electronic device fabrication due to less formation of amorphous carbon and will produce CNTs with high purities [13–14]. The properties and qualities of CNT can also be determined at the beginning of catalyst preparation. The most suitable catalyst for ACCVD technique is cobalt catalyst [6]. In previous, by decomposition in air, the oxide layer will be Co_3O_4 phase while in vacuum, Co and CoO phases could be found [15]. Hence, this report presents the analysis and extensive study on the effect of speed of spin coating and heat treatment temperatures in catalyst preparation. Subsequently, the performance of the sample selected from the

[a] *Carbon Research Technology Research Group, Faculty of Manufacturing Engineering, Universiti Teknikal Malaysia Melaka, Hang Tuah Jaya, 76100 Durian Tunggal, Melaka, Malaysia.*
† Email: asyadi@utem.edu.my
Electronic Supplementary Information (ESI) available: [details of any supplementary information available should be included here]. See DOI: 10.1039/x0xx00000x

optimum parameter was measured with CNT growth by ACCVD technique.

Experimental

Nanosized Co thin films were synthesized by using sol gel spin-coated technique. The precursor solution was prepared by diluting 42 mg of Co acetate tetrahydrate, $Co(CH_3COOCH)_2.4H_2O$, into 10 mL of absolute ethanol to produce a solution with a concentration of 16.8 mmol/L [16]. The solution was stirred vigorously for 10 min and left for 2 h, thereby leading to the formation of light pink color solution [16]. P-type silicon wafer was cut into 15 mm × 15 mm sizes. The substrates were soaked in acetone, left for 10 min sonication in ethanol, and dried by using nitrogen gas.

The precursor solution of Co acetate tetrahydrate/absolute ethanol was spin coated on the cleaned substrates at 6500, 7000, 7500, and 8000 rpm for 60 s. Subsequently, the spin-coated wafers were pre-heated at 250 °C for 1 min to vaporize the solvent, thus leaving Co catalyst thin films on the wafers. Later, the pre-heated wafers were placed in the vacuum furnace for heat treatment process of 450, 500, 550, and 600 °C to obtain Co catalyst nanoparticles.

The prepared catalyst thin film was placed in a quartz tube of the furnace for CNT growth process. The tube was evacuated using oil-free scroll pump to 0.4 Pa. To prevent the oxidation of Co catalyst, Ar gas was injected into the system at a pressure of 400 Pa concurrently with 5 min of rapid heating and 5 min of annealing process. Once the annealing process was completed, the Ar gas flow was quickly stopped, and ethanol vapor was immediately lead off into the system at flow rates of 100–150 sccm. The growth process was fixed at 2.0 kPa and 15 min of internal pressure and CVD processing time, respectively. After the growth process, the ethanol gas flow was stopped, and the samples were left for cooling to room temperature. The growth process was repeated for CVD processing temperature of 650, 675, 700, 725, and 750 °C.

The surface morphology of the sample was characterized by using field emission scanning electron microscope (FESEM, Hitachi SU8100) operated at 5 kV. The optimum parameter can be determined from the smallest and most uniform thickness of Co catalyst thin film by using FESEM. The individual CNT structure and Co nanoparticles were also characterized using a high-resolution transmission electron microscopy (HRTEM) system. TEM samples for Co on SiO_2/Si were prepared using focused ion beam (FIB) technique, and CNT samples were prepared using sonication technique. Surface chemical state analysis was conducted by X-ray photoelectron spectroscopy (XPS, Fison Instruments S-PROBE ESCA) with Al Kα (1486.6 eV) as the X-ray source. The samples were analyzed at 90° take-off angle to the surface. C 1s narrow spectrum, at 284.8 eV with chamber pressure during the measurement of 10^{-7} Pa, was used to calibrate the photoelectron binding energy (BE). The crystal structure cobalt oxide thin films were characterized by X-ray diffractometer using Cu Ka radiation in the 2theta range of 10–90 of wavelength 1.5406 A °. Raman analysis was performed by Raman spectroscopy (Uni-RAM 3500) with laser excitation of 532 nm wavelength (Nd:YAG) [17].

Results and discussion

Morphological Analysis of Co Catalyst

Spin speed is the most crucial factor to determine the success of the coated thin film. The thickness of Co catalyst thin film is gradually decreased by increasing the spin speed from 6500 rpm to 8000 rpm (Fig.1). Reportedly, the thickness of thin film could be controlled by controlling the parameter [18–19]. When the thin film is sufficiently thick, that is, more than 100 nm, the tendency for large cluster formation of Co catalyst nanoparticles is higher compared with the thin film. Co element is also known as a ferromagnetic metal [20]. Ferromagnetism is the strongest magnetism effect that has persistent magnetic moments. Co element has high tendency to be attracted by one another, thereby forming a large cluster of particles. If the thin film is sufficiently thick, the surrounding ferromagnetism effect will increase and lead to high attraction tendency. Therefore, a thinner film may help reduce the tendency for large Co cluster formation.

Co catalyst thin films are formed continuously on the substrates (Fig.1). These films are successfully formed by spin coating process. The continuity of thin film is important to ensure that Co catalyst nanoparticles are consistently formed on the substrate. Therefore, CNTs can be grown and will cover the surface substrate well. Otherwise, any carbon-based devices fabricated by these CNTs may not perform well.

(Location for Figure 1)

Fig.1 FESEM cross-sectional images of the Co catalyst thin film spin-coated on the SiO_2/Si substrates with various spin speeds; (a) 6500, (b) 7000, (c) 7500, and (d) 8000 rpm. *Note that, for clarity, only (b) is in different scale.*

The dependence of the thickness of Co catalyst thin films on the spin speed of spin coating was studied by the statistic of thin film thickness on each spin speed. As the spin speed was increased from 6500 rpm to 8000 rpm, the thin film thicknesses were decreased from 25.5 nm to 12.1 nm (Fig.2). Therefore, increasing the spin speed rotation effectively decreases the thickness of thin film deposited on silicon substrate. The thinning process is caused by the developed centrifugal force that causes shear thinning of the precursor solution to form a film layer on top of the substrate [21–22]. The thin film thickness determines the depth of the stacked particle on top of each other, which affects the surface roughness and the uniformity of particle distribution all over the surface of the substrate. If the thickness of the thin film is increased, more particles will be stacked, which causes the non-uniform particle distribution on the substrate.

The optimum distribution of Co catalyst thin film with 12.1 nm average thickness was resulted at the spin speed of 8000 rpm (Fig.2). This result was caused by the large gap between the majority and minority thicknesses. The thickness distribution for 8000 rpm was also narrower than the three other spin speeds.

Thus, Co catalyst thin film spin coated at 8000 rpm not only has the smallest thickness but also a good continuous thin film (Fig.2).

(Location for Figure 2)

Fig.2 Average thickness analysis of Co thin films at different spin speeds.

In sol–gel process, heat treatment process is crucial to obtain a firm and stable shape and state of the thin film [23–24]. During the heat treatment process, the nanoparticles tend to form from the thin film surface. The temperature and duration of heating for the Co catalyst thin film are needed to control so that the spin-coated Co catalyst thin film structure will not turn into crystalline structure. Once the crystalline structure is formed, the structure is in stable state; thus, it is not reactive and will not function as catalyst for CNT growth.

Based on the FESEM images in Fig.3, Co catalyst nanoparticles are successfully formed on the SiO_2/Si substrate. No large agglomerated particles were formed on the substrate surface.

Diameter analysis of as-prepared Co nanoparticles is also shown in Fig.4, supported by the HRTEM observation result. The particle size distribution trend for post-heat treatment temperature of 450 °C with the 30 measured particles, *n*=30, was more similar to a normal distribution compared with the other post-heat treatment temperatures. The normal distribution for that particular histogram showed that the majority size of particles for that sample was at 10.64 nm (Fig.4 (a). The particle size distribution for post-heat treatment temperature within the range of 500–600 °C showed a fluctuating trend (Figs. 4(b)–4(d)). Based on this trend, the distribution of tube diameter of CNTs grown on those nanoparticles is considered fluctuating as well. Therefore, the post-heat treatment temperature of 450 °C is the optimum temperature for Co catalyst nanoparticle formation, which would lead to a good distribution of the CNT tube size.

Based on the enlarged images at the right top corner of every image, the size of Co catalyst nanoparticle is slightly increased by the increasing post-heat treatment temperature. The changes in Co catalyst nanoparticles size are affected by the increment of post-heat temperatures. Hence, post-heat temperature is a critical factor that should be controlled to control the desired size of catalyst nanoparticles. The average size of Co catalyst nanoparticles increases with increasing post-heat temperature. The smallest average diameter of Co catalyst nanoparticles with a diameter of 10.64 nm was found at post-heat treatment of 450 °C (Fig.4 (e)). This value was confirmed by HRTEM with a diameter approximately 10.67 nm. Meanwhile, the largest average size of Co catalyst nanoparticles was at post-heat temperature of 600 °C. Additionally, Co catalyst nanoparticles formed at different post-heat treatment temperatures were round in shape (Fig.4 (f)).

In principle, a particle needs a specific energy to turn from gel state into particle state. If excess energy is present in the system, that energy would then turn the small particle into a large particle. When the size of the particle reaches its limit, then the grain of that particular particle would open up and form a necking; subsequently, the particle combines with the particle next to it. If this phenomenon occurs, the crystalline structure could be obtained [25]. Therefore, to prevent this phenomenon, determining an optimum temperature for Co catalyst nanoparticle formation is crucial. In the present study, 450 °C is the optimum post-heat treatment temperature for Co catalyst nanoparticle formation.

(Location for Figure 3)

Fig.3 FESEM top view images of Co catalyst nanoparticles from various post-heat treatment temperatures: (a) 450, (b) 500, (c) 550, and (d) 600 °C. *Note that, for clarity, only (a) is in different scale.*

(Location for Figure 4)

Fig.4 Diameter analysis of Co catalyst nanoparticles with post-heated at (a) 450, (b) 500, (c) 550, and (d) 600 °C; (e) average particle size of Co catalyst nanoparticles at four different post-heat treatments; (f) HRTEM image of Co nanoparticles on SiO_2 based (sample preparation using FIB).

Surface Properties of Co Catalyst Films and Nanoparticles

Surface Chemical States of Co by XPS

Further analysis on the surface chemical states of the pre-heated samples was conducted by XPS analysis. Co 2p region was present in the survey spectrum (Fig.5(a)). The primary signals of Co 2p region came from 793 (Co $2p_{1/2}$) and 778 eV (Co $2p_{3/2}$) (Fig.5(b)). Both primary spin-orbits BE were separated by 15 eV. Co has two types of species: Co^{2+} and Co^{3+}. These two types are difficult to be differentiated by BE values.

The Co $2p_{3/2}$ XPS spectrum of CoO compound consists of a broad main peak and very intense shake-up satellite [26]. Shake-up satellite is the peak that exhibits a shoulder at both primary spin-orbit sides [27]. This peak is used as a fingerprint for the recognition of high-spin Co(II) species in CoO [27–28]. The shake-up satellite found at Co $2p_{3/2}$ spin-orbital is intense because it can be clearly seen in the narrow spectrum; this satellite is located at about 4.4 eV above the primary Co $2p_{3/2}$ peak. Thus, it is suggested that CoO compound is present in the pre-heated samples, and the XPS spectrum behavior indicates the post heated catalyst Co nanoparticles are Co metal covered by CoO shell, [29].

(Location for Figure 5)

Fig.5 XPS spectra of the pre-heated Co catalyst films for (a) survey spectrum and (b) narrow spectrum of Co 2p of Co oxide system. Note that asterisks * represent the shake-up satellite peaks of Co 2p.

Co 2p region was also observed in the survey spectrum of Co catalyst nanoparticles (Fig.6 (a)). The primary spin-orbital of BE came from 794.8 (Co $2p_{1/2}$) and 778.8 eV (Co $2p_{3/2}$) (Fig.6 (b)). Both signals were separated by 16 eV. The difference value is consistent with previous study [27, 30]. The shake-up satellite observed at Co $2p_{3/2}$ spin-orbital is less intense as it almost disappears in the narrow spectrum; this satellite is located about 3.7 eV above the primary Co $2p_{3/2}$ peak.

By comparing the Co 2p narrow spectra of Co catalyst thin film (pre-heated Co) and Co catalyst nanoparticles (post-heated Co), the Co $2p_{3/2}$ shake-up satellite of the pre-heated Co was observed to be more intense compared with the post-heated Co (Fig.7). The intensity difference in both shake-up satellites confirmed that Co_3O_4 compound is present in the post-heated Co. This result is supported by a report mentioning that the Co $2p_{3/2}$ of Co_3O_4 compound consists of much smaller shake-up satellite compared with that of the CoO compound [26]. Hence, these findings support the previous findings that CoO and Co_3O_4 compounds are present on both pre-heated Co catalyst thin film and post-heated Co catalyst nanoparticles, respectively.

(Location for Figure 6)

Fig.6 XPS spectra of the post-heated Co catalyst nanoparticles for (a) survey spectrum and (b) narrow spectrum of Co 2p of Co oxide system. Note that asterisks * represent the shake-up satellite peaks of Co 2p.

(Location for Figure 7)

Fig.7 Comparison of Co 2p narrow spectra for pre-heated and post-heated Co samples. Note that asterisks * represent the shake-up satellite peaks of Co 2p.

Co Crystal Structure Analysis byXRD

Structural identification and changes in the crystallinity of Co were studied by using X-ray diffraction (XRD) technique. XRD patterns of cobalt oxide thin films with different post-heated temperatures and constant pre-heated and annealed temperatures are shown in Fig.8. First, all samples confirming XRD peak of SiO_2 substrate- Si (112) as reference [31]. XRD peaks corresponding to Co oxide were observed at pre-heated and post-heated samples as CoO and Co_3O4 cubic phases but with a very low intensities and broad peaks. These peaks are consistent with that of XRD analysis reported by Koshizaki's group [32]. This result also corresponds to the fact that Co oxide film showed a semicrystalline structure rather than the amorphous nature [33].

(Location for Figure 8)

Fig.8 XRD patterns of Co samples prepared on SiO_2/Si substrates at various post-heated and constant pre-heated temperatures.

CNT Growth by Alcohol Catalytic CVD

CNT Structural Analysis by Raman Spectroscopy

ACCVD technique has high potential to produce good quality CNT with less amount of amorphous carbon. Moreover, this technique has wide substrate selectivity, good economic value, and high yield of catalytic reaction. ACCVD has also been selected to grow CNT from the spin-coated Co catalyst nanoparticles. The CNT quality was determined by the I_G/I_D ratio value; meanwhile, from the radial breathing mode (RBM), the presence of single-walled CNT (SWCNT) and its tube diameter can be detected and measured accordingly. Fig.9 shows the Raman spectra for CNT grown on the spin-coated Co catalyst nanoparticles at CVD processing temperatures of 650, 675, 700, 725, and 750 °C. Based on the broad range of Raman spectra, specifically within the range of 50–2000 cm^{-1}, the G-band, D-band, Si band, and RBM peaks were detected. The highest intensity in the spectra at 520 cm^{-1} belonged to Si, which was confirmed by the reference blank substrate spectrum. G-band, which had higher intensity compared with D-band (1319–1330 cm^{-1}), was detected at 1592–1594 cm^{-1} Raman shift for all CVD processing temperatures. In previous studies, the G- and D-bands are normally present within the range of 1580–1600 and 1310–1335 cm^{-1} of Raman shift, respectively [25, 34–35]. At this stage, CNT is successfully grown on the spin-coated Co catalyst nanoparticles.

RBM peaks could be found within the range of 100–400 cm^{-1} Raman shift [4, 36]. It is a finger print for the presence of SWCNTs and DWCNTs in Raman spectrum [36]. The presence of RBM region in the Raman spectrum shows that SWCNT is present on the samples [38]. In the plotted Raman spectra, RBM peaks were detected within the range of 169–335 cm^{-1} Raman shift (Fig.9 (a)). To initiate the growth of SWCNT or DWCNT, the catalyst particles should be sufficiently small, with a diameter or DWCNT inner diameter of 1–2 nm [39]. Although in total the Co catalyst nanoparticles found in the average diameter of 10.64 nm, smaller Co nanoparticles were also presence as evidenced from Raman analysis. Confirmation of CNT structures will be discussed in later part of this manuscript.

The intensity of D-band was much lower than that of G-band (Fig.9 (c)); the height of the former was about a quarter of the latter. By increasing the CVD processing temperature from 650 °C to 700 °C, the G-band intensities were increased accordingly. Meanwhile, when the CVD processing temperature was increased up to 750 °C, the G-band intensities were decreased; the same trend applies to D-band intensities. The D-band indicates the amorphous content in the samples, whereas the G-band corresponds to the tangential modes of graphitic planes in CNTs [4, 40]. Thus, the carbon was highly graphitized at the CVD processing temperature of 700 °C.

Another peak at the left shoulder of G-band at Raman shift of around 1550 cm^{-1} was observed (Fig.9 (c)). The presence of this peak, which was labeled as G_1-band, was found at the Raman spectrum of all CVD processing temperatures. This characteristic, similar to RBM, was specific to SWCNT. Normally, G_1-band could be observed when the particular samples were inspected by the excitation energy in green or blue range of visible light. This peak could also be detected when the typical tube diameters were around 1.4 nm [41]. Therefore, along with the presence of RBM region, this G_1-band could be used to confirm that SWCNTs are grown on the spin-coated Co catalyst nanoparticles.

(Location for Figure 9)

Fig.9 (a) Raman results within the broad range of 50–1800 cm^{-1} Raman shift; (b) RBM area of the CNTs grown (within the range of 100–400 cm^{-1}); and (c) D- and G-bands of Raman peaks for CNT grown at various CVD processing temperatures.

The I_G/I_D ratio is used as an indicator to determine the quality of the as-grown CNTs. By increasing the CVD processing temperature

from 650 °C to 700 °C, the I_G/I_D ratio was also increased (Fig.10). However, the ratio values were decreased when the CVD processing temperature was increased up to 750 °C. Higher I_G/I_D ratio value indicates that the as-grown CNTs have good quality and low amount of defects. The highest I_G/I_D ratio calculated shows that the optimum temperature to grow good quality CNTs by ACCVD technique is at CVD processing temperature of 700 °C.

$$I_G/I_D \text{ ratio} = \text{G-band intensity} / \text{D-band intensity} \quad \text{(Eq.1)}$$

The RBM region was found within the range of 100–400 cm^{-1} (Fig.9 (b)). In the RBM region, nine obvious peaks were observed; the 8th peak belongs to the Si peak. Moreover, two dominant peaks, namely, 5th and 6th peaks were also present in the RBM region. These two peaks were the strongest peaks at the CVD processing temperature of 700 °C compared with the other CVD processing temperatures. These two dominant peaks consistently appeared at all CVD processing temperatures, thus the dominant peaks were confirmed to belong to the CNTs grown on the spin-coated Co catalyst nanoparticles with the spin speed of 8000 rpm and post-heat treatment temperature of 450 °C by ACCVD technique. The CVD processing temperature of 700 °C was confirmed as the optimum CVD processing temperature to grow good quality SWCNTs. These findings are significant to the statement that Co is a superior catalyst in SWCNT growth [42–44].

(Location for Table 1)

Table 1 I_G/I_D ratios of the as-grown CNT grown at various CVD processing temperatures.

(Location for Figure 10)

Fig.10 The I_G/I_D ratios the as-grown CNTs at different CVD temperatures.

Further, SWCNT diameter was not affected by the increase of CVD processing temperatures (Fig.11). The tube diameter of as-grown SWCNT is dependent on the catalyst nanoparticle size [4, 45]. Moreover, SWCNT growth could be initiated by the catalyst particles as small as 1–2 nm in diameter. The as-grown CNT tube diameter may be the same size or less as the size of catalyst nanoparticles. The calculated SWCNT tube diameters were within the range of 0.75–1.48 nm, which was less than 2 nm; therefore, a part of the Co catalyst nanoparticle size during the growth process was also within that range.

$$\text{SWCNT diameter, } d_{tube} = 248 / \text{RBM} \quad \text{(Eq.2)}$$

SWCNTs with smaller tube diameter have good potential for application in electronic devices [46–48]. The SWCNT tube diameters measured in this study were around 1.4 nm or less. Moreover, the G-band has the left shoulder of the dominant G-band, another peak called G_1-band. This peak could be analyzed when the typical tube diameter is around 1.4 nm [41].

(Location for Figure 11)

Fig.11 Statistical analysis of SWCNTs average diameter with varied CVD processing temperatures. Inset is the table for the analysis.

Confirmation of CNT structures from HRTEM

High resolution TEM was applied to investigate the morphology of the CNTs synthesized by ACCVD over the Co catalyst (Fig.12). It was found that the samples consisted exclusively of agglomerates of CNTs (Fig.12 (a)). The CNTs were grown randomly aligned like spaghetti structure (Fig.12 (b)). The measured length of CNT is around 900 nm. In the Raman analysis, it was suggested that the RBM peaks showed the presence of SWCNTs. It is also known that RBM peaks also could be exhibited when there is DWCNT presented during the analysis. DWCNT structure was found in high resolution TEM analysis (Fig.12 (c)). The average outer and inner diameter is 4.1 nm and 2.9 nm, respectively. This finding showed that the Co nanoparticles have the size of around 10 nm. In addition, the presence of MWCNT with the Co catalyst inside the tube was found in Fig.12 (d). The average of outer and inner diameter of MWCNT structure is 10.7 nm and 2.7 nm, accordingly. With this, it can be concluded that growth mode for the CNTs was the tip-growth mode and is consistent with previous work using the similar ACCVD system [49].

(Location for Figure 12)

Fig.12 HRTEM observations of (a) mixture/agglomerated CNTs, (b) spaghetti-like of CNT structure and its length, (c) DWCNT structure and (d) confirmation of tip-growth mode of CNT.

Conclusions

In conclusion, Co catalyst particles with less than 20 nm could be achieved by spin coating process. The thickness of the catalyst thin films could be controlled by controlling the speed of spin coating. When the spin speed was increased, the thickness was decreased because of shear thinning. Meanwhile, the catalyst particle size could be controlled by controlling the heat treatment temperature. For particle formation, when the heat treatment temperature was increased, the particle size became larger because of cluster formation. Therefore, the particle size and film thickness could be controlled by determining the suitable parameter for spin speed and heat treatment temperature.

Acknowledgements

The authors are grateful to the financial support by the Ministry of Higher Education of Malaysia, under the Exploratory Research Grant Scheme with research grant number ERGS/1/2013/TK04/UTEM/02/01/E00032.

References

1 M. A. Azam, N. S. A. Manaf, E. Talib and M. S. A. Bistamam, *Ionics*, 2013, **19**, 1455.
2 N. S. A. Manaf, M. S. A. Bistamam and M. A. Azam, *ECS J. Solid State Sci. Technol.*, 2013, **2**, M3101.
3 M. A. Azam, M. W. Abd Rashid, K. Isomura, A. Fujiwara and T. Shimoda, *Adv. Mater. Res.*, 2012, **620**, 213.
4 C.-M. Seah, S.-P. Chai, S. Ichikawa and A. R. Mohamed, *Carbon*, 2012, **50**, 960.
5 M. Kumar and Y. Ando, *J. Nanosci. Nanotech.*, 2010, **10**, 3739.
6 M. Abu-Abdeen and A. A. Aljaafari, *Mater. Sci. App.*, 2011, **2**, 922.
7 Y. Murakami, Y. Miyauchi, S. Chiashi and S. Maruyama, *Chem. Phys. Lett.*, 2003, **377**, 49.
8 B. Bräuer, D. R. T. Zahn, T. Rüffer and G. Salvan, *Chem. Phys. Lett.*, 2006, **432**, 226.
9 B. W. Shivaraj, H. N. Narasimha Murthy, M. Krishna and S. C. Sharma, *Int. J. Thin Film. Sci. Technol.*, 2013, **2**, 143.
10 Y. Murakami, Y. Chiashi, Y. Miyauchi, M. Hu, M. Ogura, T. Okubo and S. Maruyama, *Chem Phys Lett.*, 2004, **385**, 298.
11 H. Sugime, S. Noda, S. Maruyama and Y. Yamaguchi, *Carbon*, 2009, **47**, 234.
12 M. A. Azam, K. Isomura, A. Fujiwara and T. Shimoda, *Phys. Status. Solidi. A.*, 2012, **209**, 2260.
13 N. Inami, M. A. Mohamed, E. Shikoh and A. Fujiwara, *Sci. Tech. Adv. Mater.*, 2007, **8**, 292.
14 T. Izak, T. Danis, M. Vesely, M. Marton and M. Michalka, *Vacuum*, 2008, **82**, 134.
15 P. Baraldi, *Spectrochim. Acta*, 1983, **38A**, 51.
16 M. Abu-Abdeen, *Mater. Sci. Appl.*, 2011, **2**, 922.
17 M. A. Azam, M. A. Mohamed, E. Shikoh and A. Fujiwara, *Jpn. J. Appl. Phys.*, 2010, **49**, 02BA04.
18 G. A. Luurtsema, *Dissertation*, 1997, University Of California, Berkeley.
19 B. W. Shivaraj, H. N. N. Murthy, M. Krishna and S. C. Sharma, *Int. J. Thin Films Sci. Techn.*, 2013, **2**, 143.
20 W. Gong, H. Li, Z. Zhao and J. Chen, *J. Appl. Phys.,* 1991, **69**, 5119.
21 D. B. Hall, P. Underhill and J. M. Torkelson, *Polym. Eng. Sci.*, 1998, **38**, 2039.
22 D. E. Bornside, C. W. Macosko and L. E. Scriven, *J. Imaging Technol.*, 1987, **13**, 122.
23 S. A. Kamaruddin, K.-Y. Chan, H.-K. Yow, M. Z. Sahdan, H. Saim and D. Knipp, *Appl. Phys. A. Mater.*, 2011, **104**, 263.
24 J. Li, J. Xu, Q. Xu and G. Fang, *J. Alloy Compd.*, 2012, **542**, 151.
25 K.-S. Kim, W.-R Myung and S.-B. Jung, *Electron Mater. Lett.*, 2012, **8**, 309.
26 V.M. Jiménez, A. Fernáindez, J.P. Espinós and A.R. Gonzádez-Elipe, *J. Electron Spectrosc.*, 1995, **71**, 61.
27 D. Barreca and C. Massignan, *Chem. Mater.*, 2001, **13**, 588.
28 J. Haber and L. Ungier, *J. Electron Spectrosc.*, 1997, **12**, 305.
29 H. T. Yang, C. M. Shen, Y. G. Wang, Y. K. Su, T. Z. Yang and H. J. Gao, *Nanotech.*, 2004, **15**, 70.
30 M. A. Azam, A. Fujiwara and T. Shimoda, *Appl. Surf. Sci.*, 2011, **258**, 873.
31 H. Schulz, W. Denner and H. d'Amour, *Acta Crystallogr. B*, 1979, **35**, 550.
32 N. Koshizaki, A. Narazaki and T. Sasaki, *Scripta Mater.,* 2001, **44**, 1925.
33 S.G. Kandalkar, J.L. Gunjakar and C.D. Lokhande, *Appl. Surf. Sci.*, 2008, **254**, 5540.
34 A. Mahmoodi, M. Ghoranneviss, M. Mojtahedzadeh, S. H. H. Hosseini and M. Eshghabadi, *Int. J. Phys. Sci.*, 2012, **7**, 949.
35 H. R. Barzegar, F. Nitze, T. Sharifi, M. Ramstedt, C. W. Tai, A. Malolepszy, L. Stobinski and T. Wågberg, *J. Phys. Chem. C.*, 2012, **116**, 12232.
36 C. Portet, P. L. Taberna, P. Simon and E. Flahaut, *J. Power Sources*, 2005, **139**, 371.
37 H. Kim, J. Kang, Y. Kim, B. H. Hong, J. Choi and S. Iijima, *J. Nanosci. Nanotech.*, 2011, **11**, 470.
38 S. Noda, K. Hasegawa, H. Sugime, K. Kakehi, Z. Zhang, S. Maruyama and Y. Yamaguchi, *Jpn. J. Appl. Phys.*, 2007, **46**, L399.
39 L. I. Wei, B. O. Wang, D. Liu and L. Li, *World Scientific*, 2009, **4**, 99.
40 H. Kim, J. Kang, Y. Kim, B. H. Hong, J. Choi and S. Iijima, *J. Nanosci. Nanotechn.*, 2011, **11**, 470.
41 S. Reich, C. Thomson and J. Maultzsch, 1st Ed, Weinhem: WILEY-VCH.
42 S. M. Bachilo, L. Balzano, J. E. Herrera, F. Pompeo, D. E. Resasco and R. B. Weisman, *J. Am. Chem. Soc.*, 2003, **37**, 11186.
43 Y. Chen, D. Ciuparu, S. Y. Lim, Y. H. Yang, G. L. Haller and L. Pfefferle, *J. Catal*, 2004, **2**, 453.
44 Y. Chen, D. Ciuparu, S. Lim, Y. H. Yang, G. L. Haller and L. Pfefferle, *J. Catal*, 2004, **2**, 351.
45 H. Dai, A. G. Rinzler, P. Nikolaev, A. Thess, D. T. Colbert and R. E. Smalley, *Chem. Phys. Lett.*, 1996, **260**, 471.
46 K. H. An, K. K. Jeon, J. K. Heo, S. C. Lim, D. J. Bae and Y. H. Lee, *J. Electrochem. Soc.*, 2002, **149**, A1058.
47 K. H. An, W. S. Kim, Y. S. Park, Y. C. Choi, S. M. Lee, D. C. Chung, D. J. Bae, S. C. Lim and Y. H. Lee, *Adv. Mater.*, 2001, **13**, 497.
48 K. H. An, W. S. Kim, Y. S. Park, J.-M. Moon, D. J. Bae, S. C. Lim, Y. S. Lee and Y. H. Lee, *Adv. Func. Mater.*, 2001, **11**, 387.
49 M. S. A. Bistamam and M. A. Azam, *Res. Phys.*, 2014, **4**, 105.

Figure 1

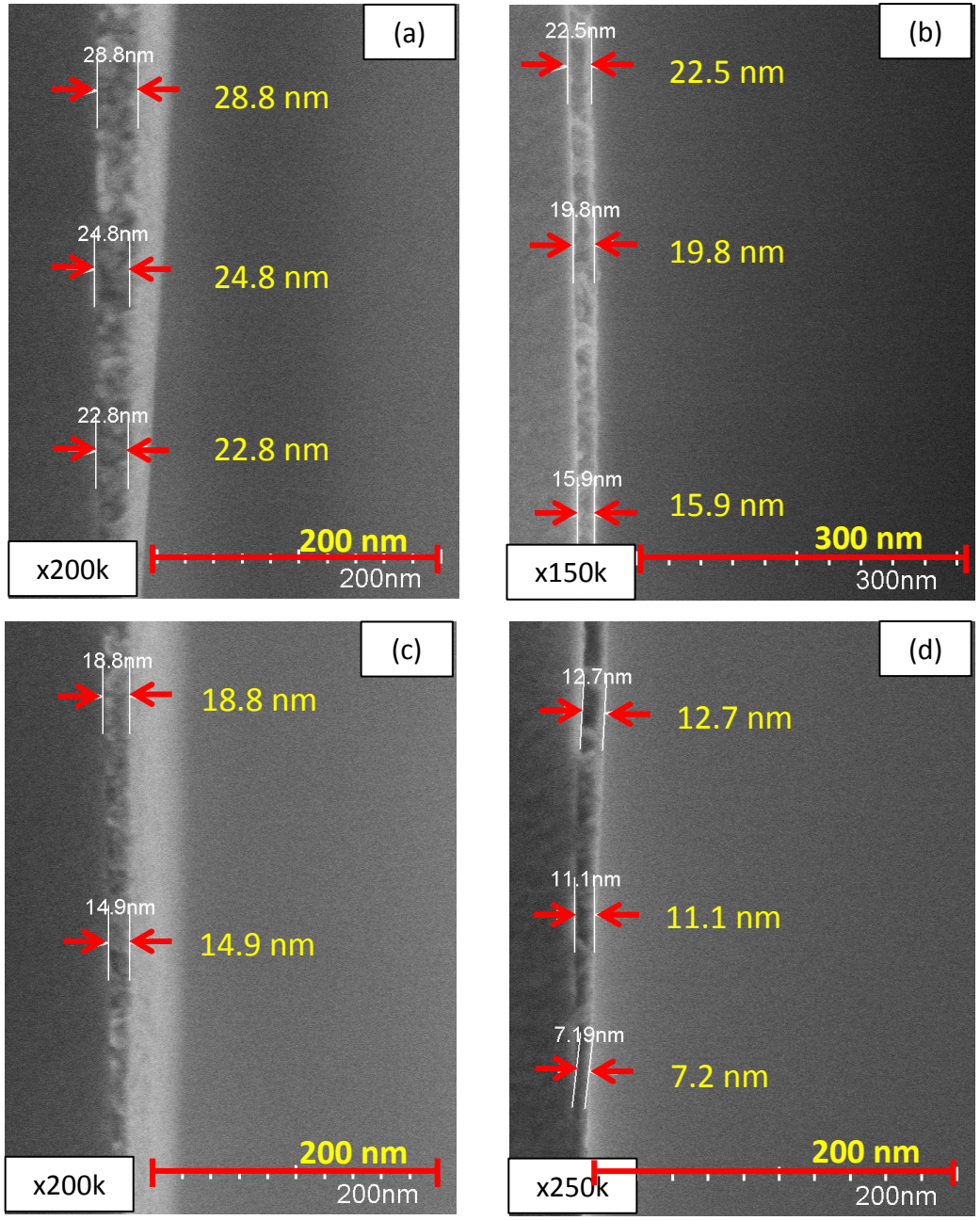

Figure 2

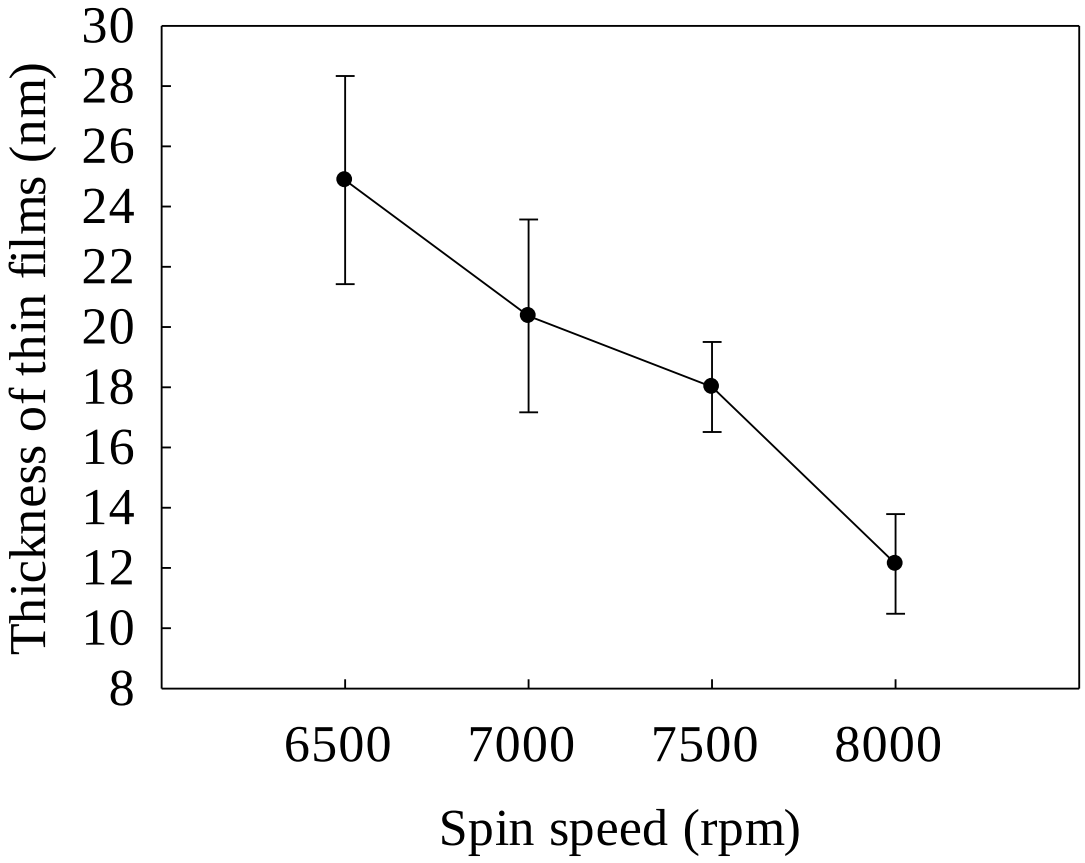

Figure 3

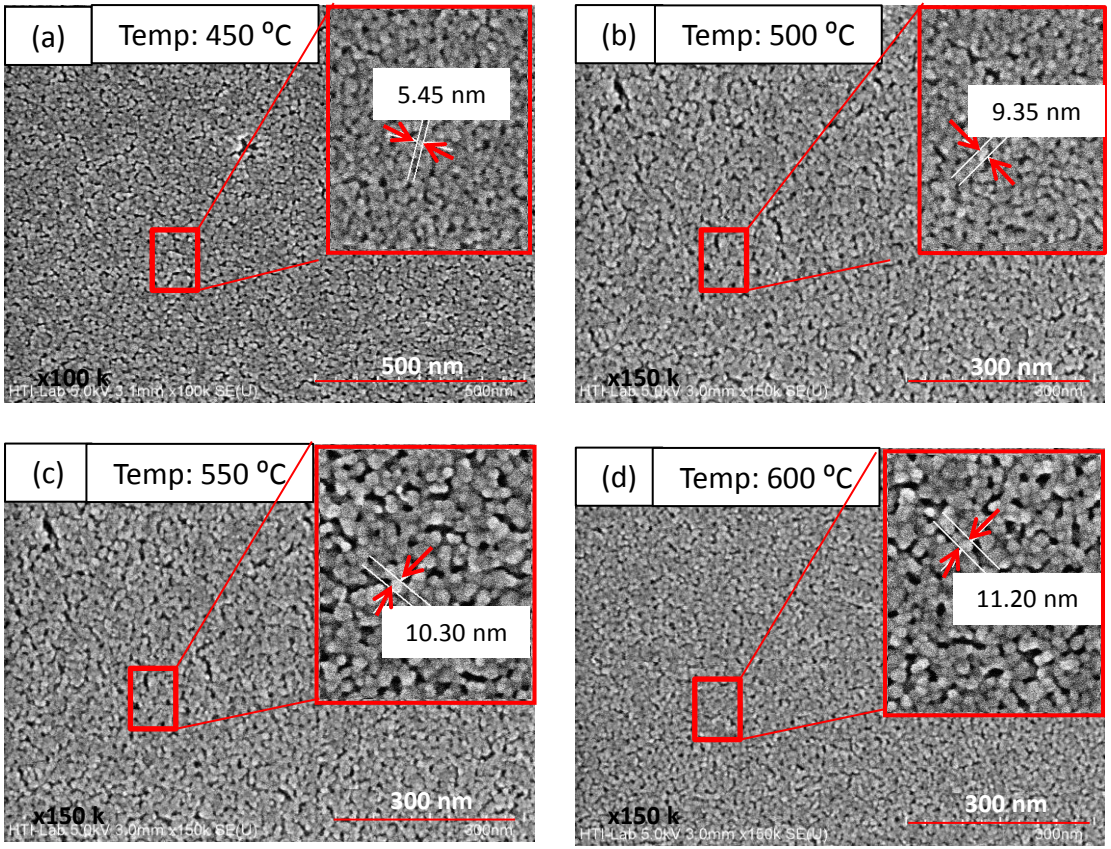

Figure 4

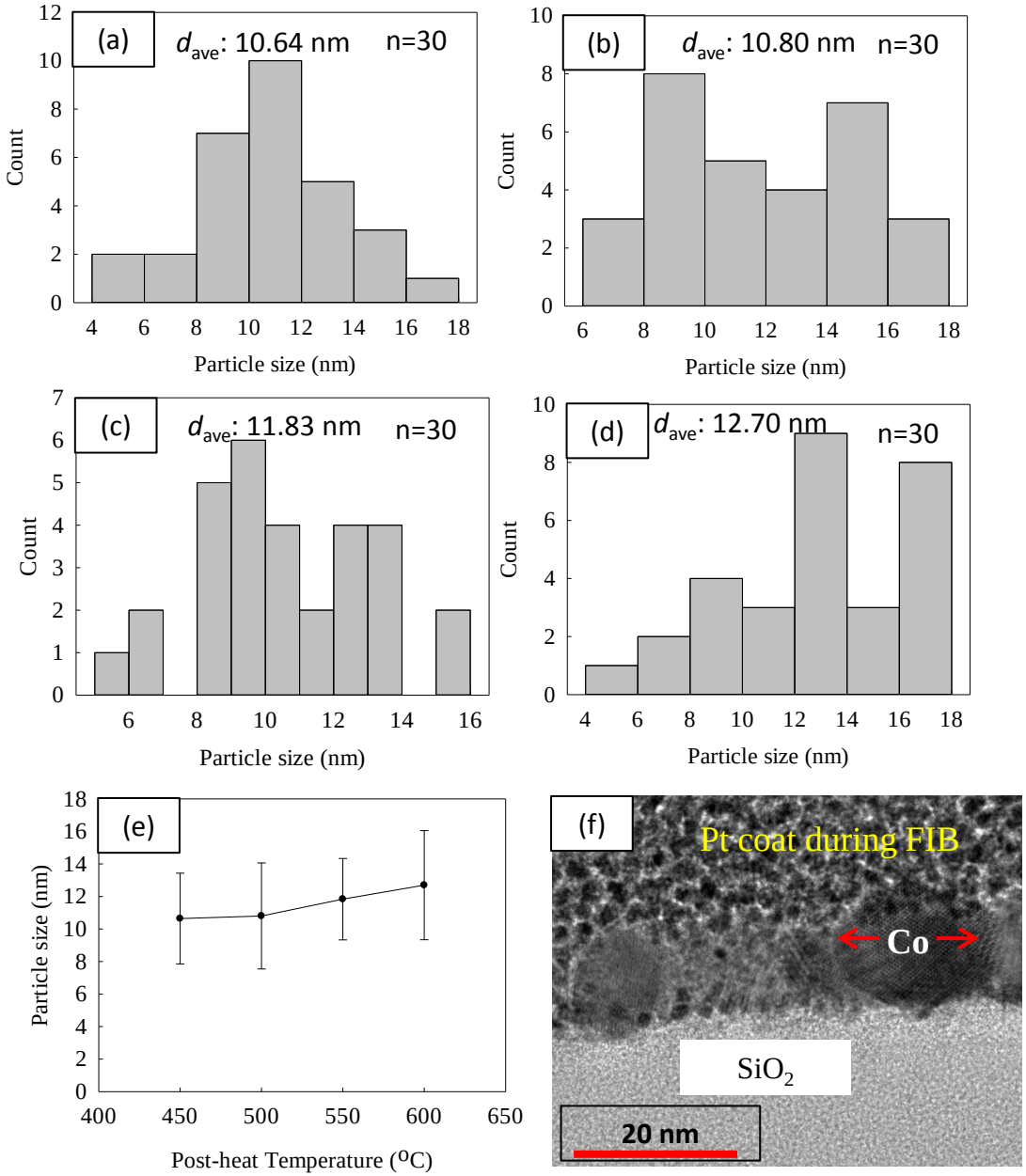

Figure 5

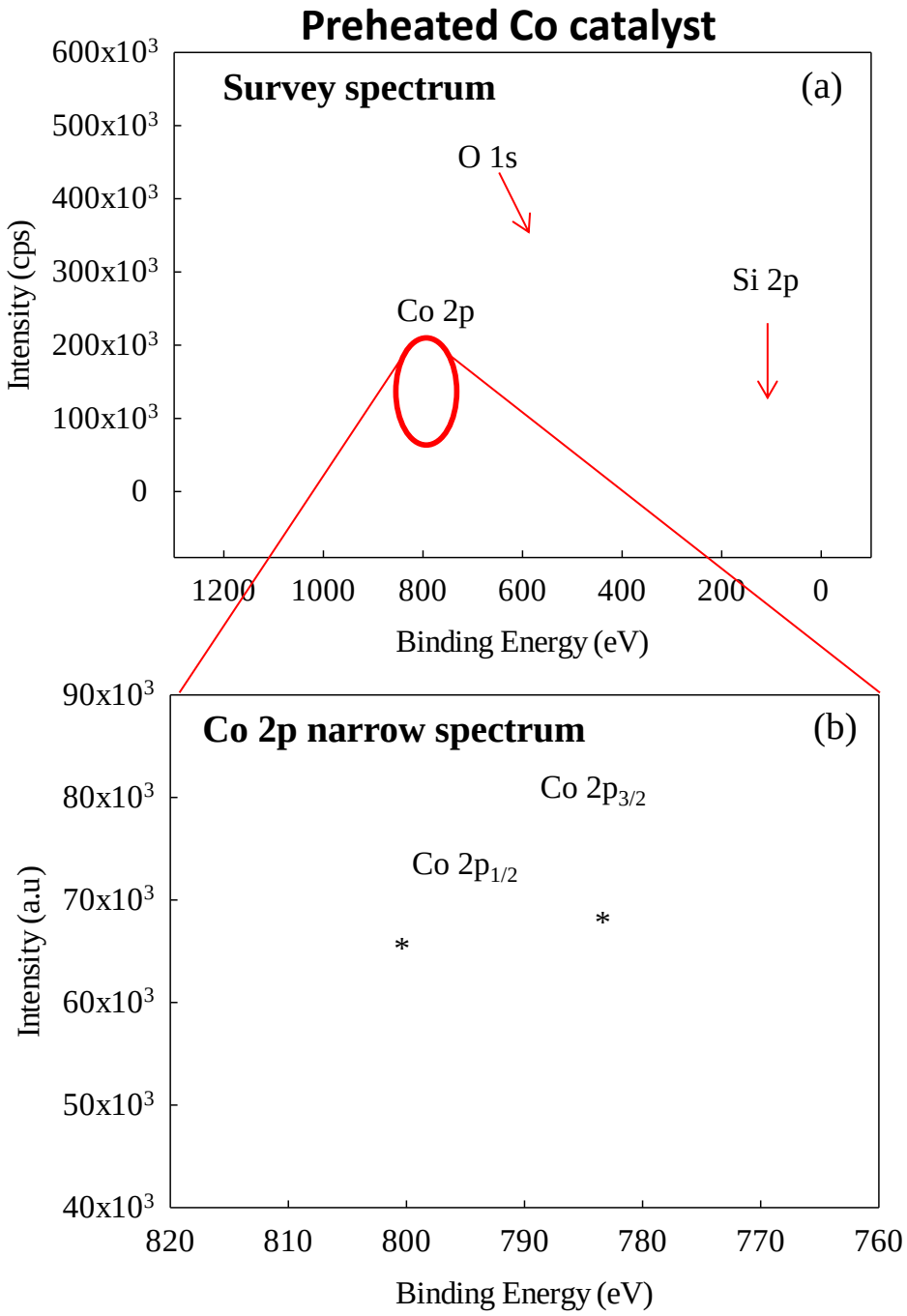

Figure 6

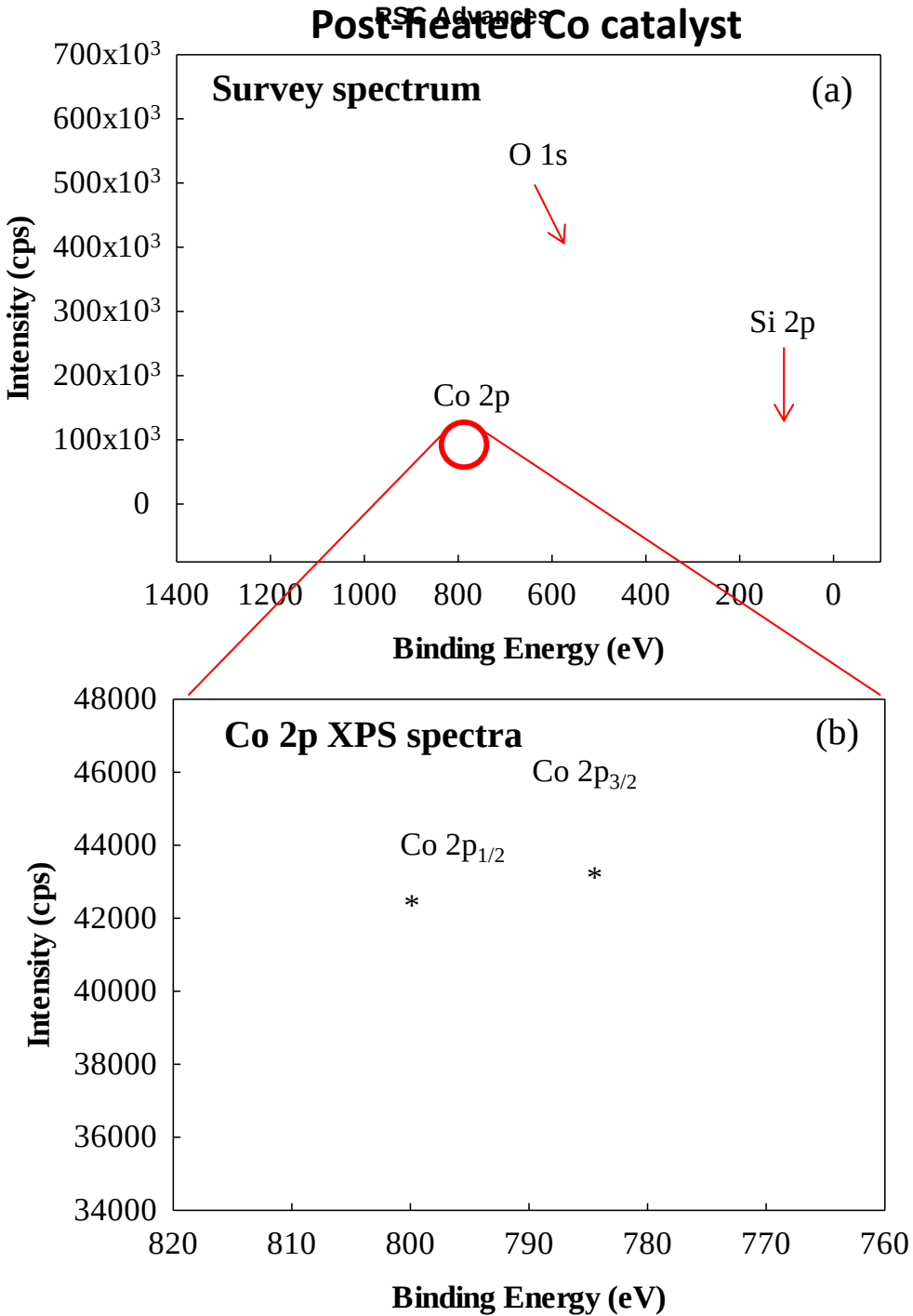

Figure 7

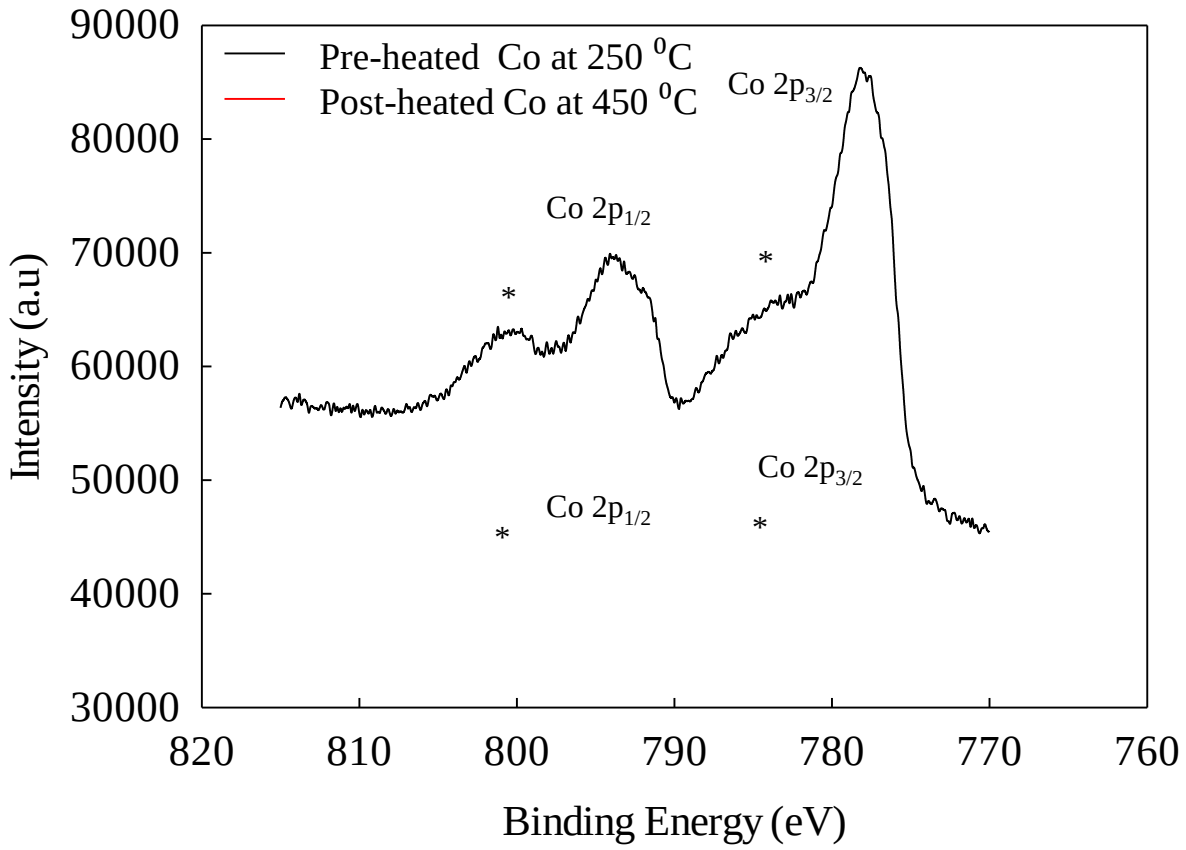

Figure 8

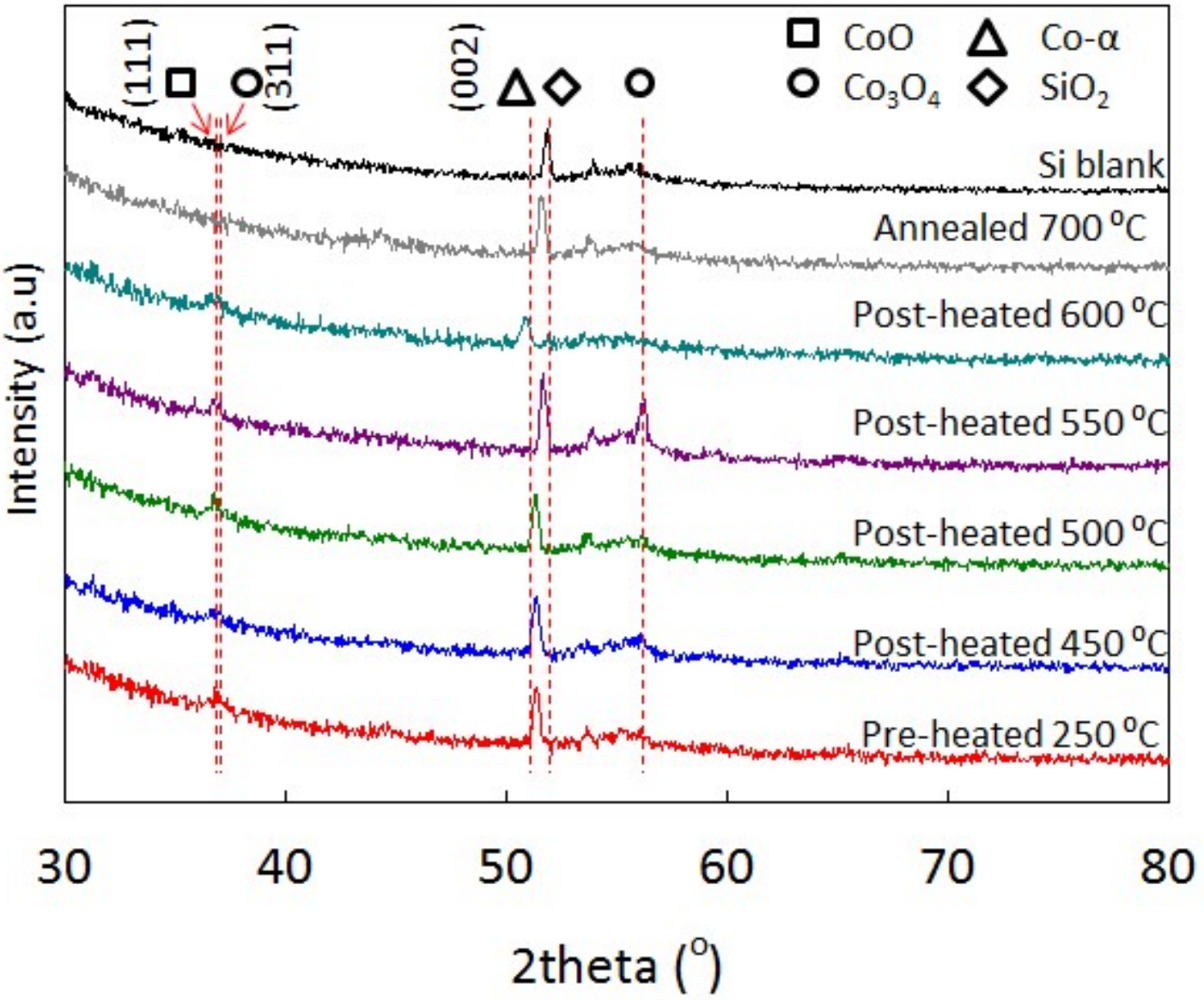

Figure 9

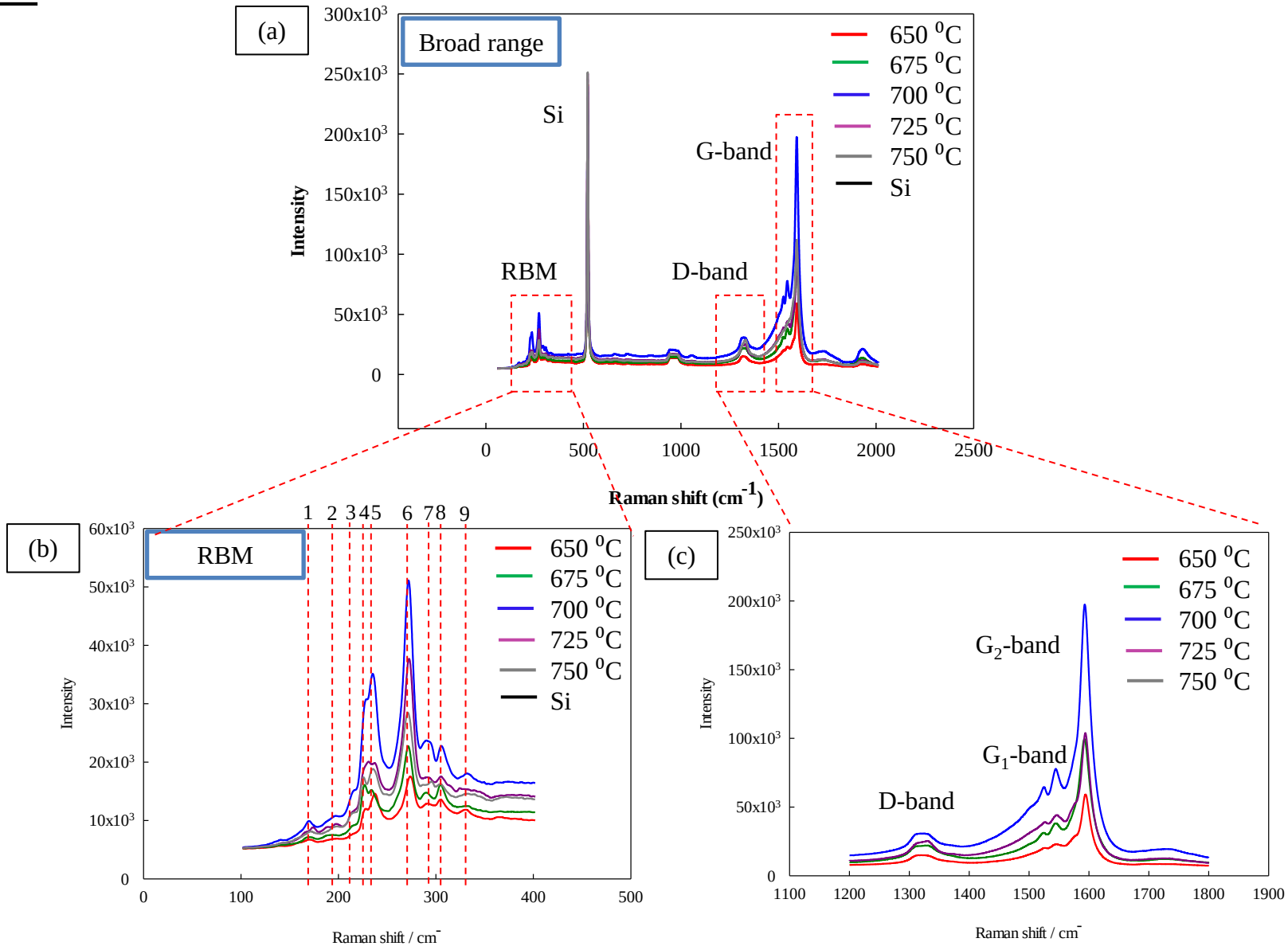

Figure 10

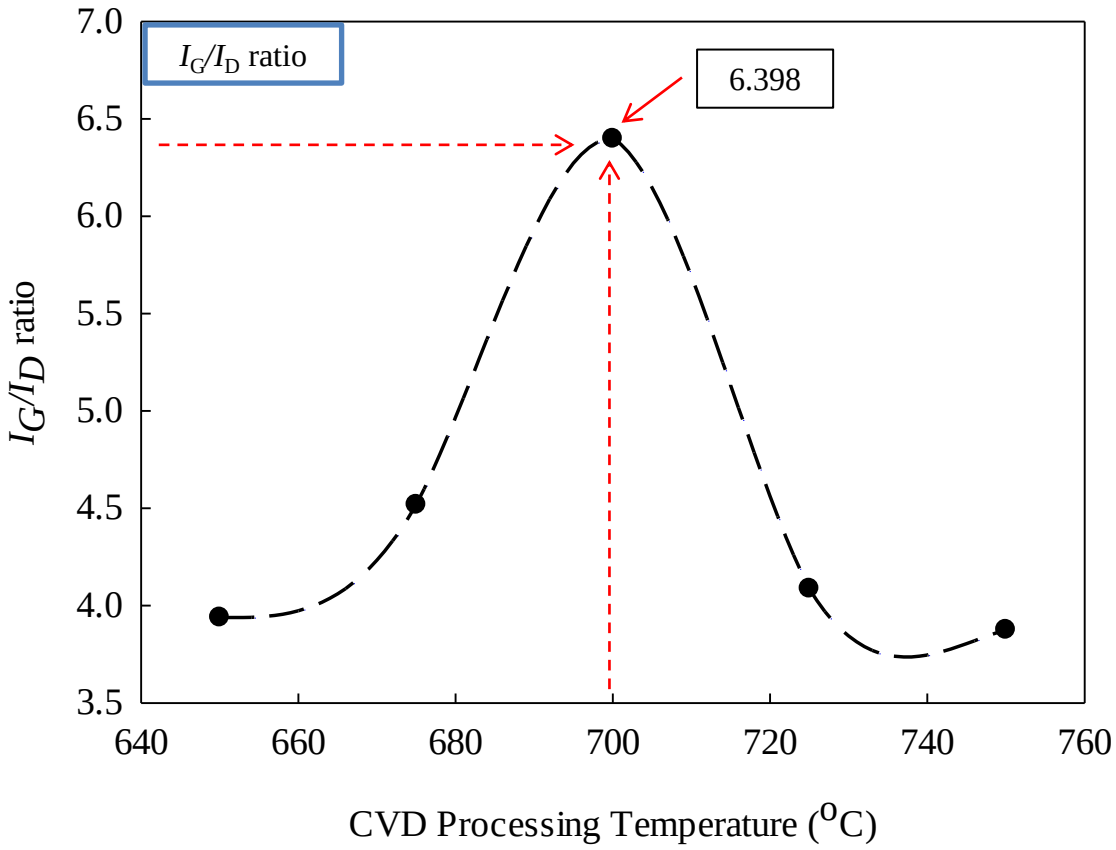

Figure 11

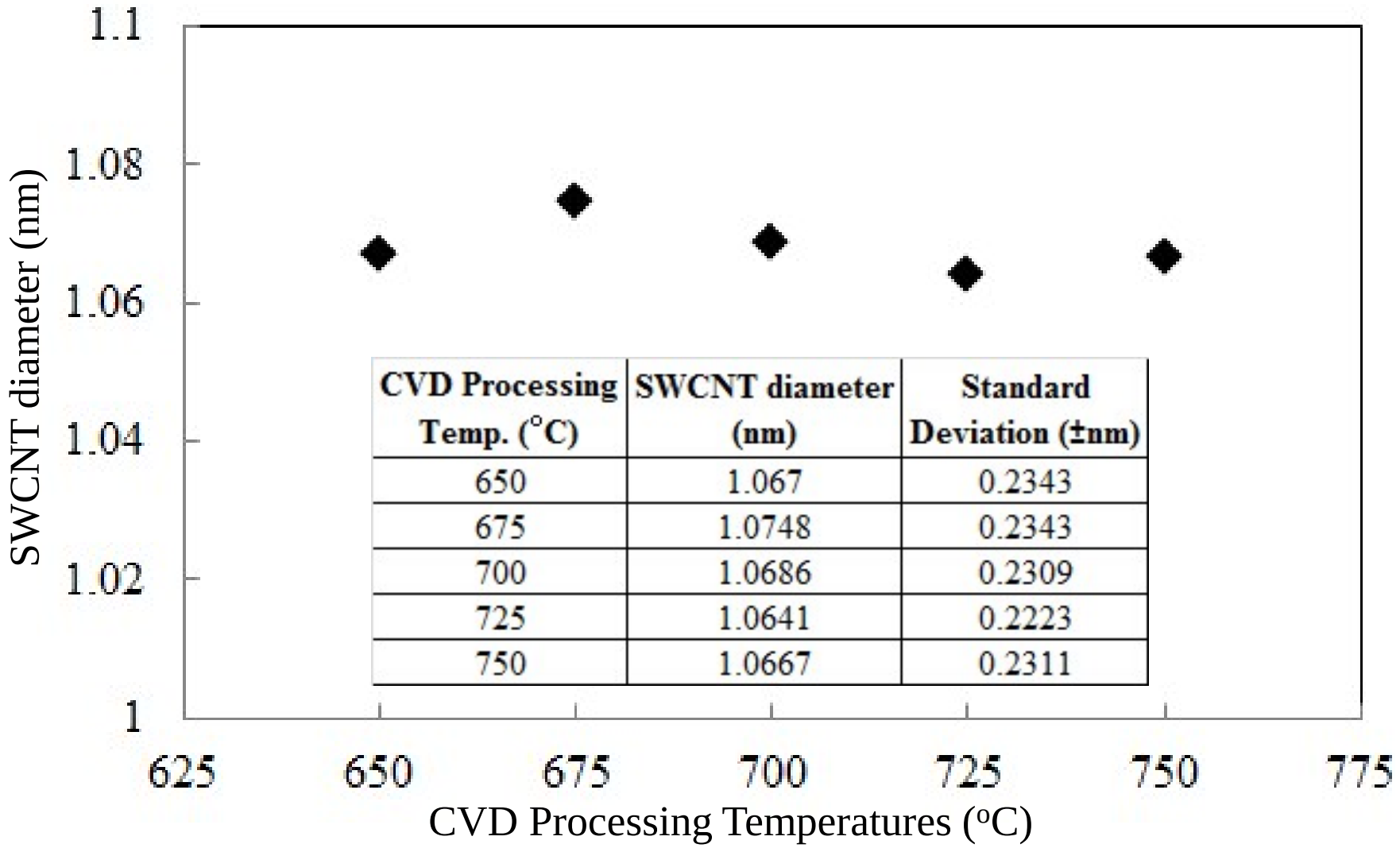

CVD Processing Temp. (°C)	SWCNT diameter (nm)	Standard Deviation (±nm)
650	1.067	0.2343
675	1.0748	0.2343
700	1.0686	0.2309
725	1.0641	0.2223
750	1.0667	0.2311

Figure 12

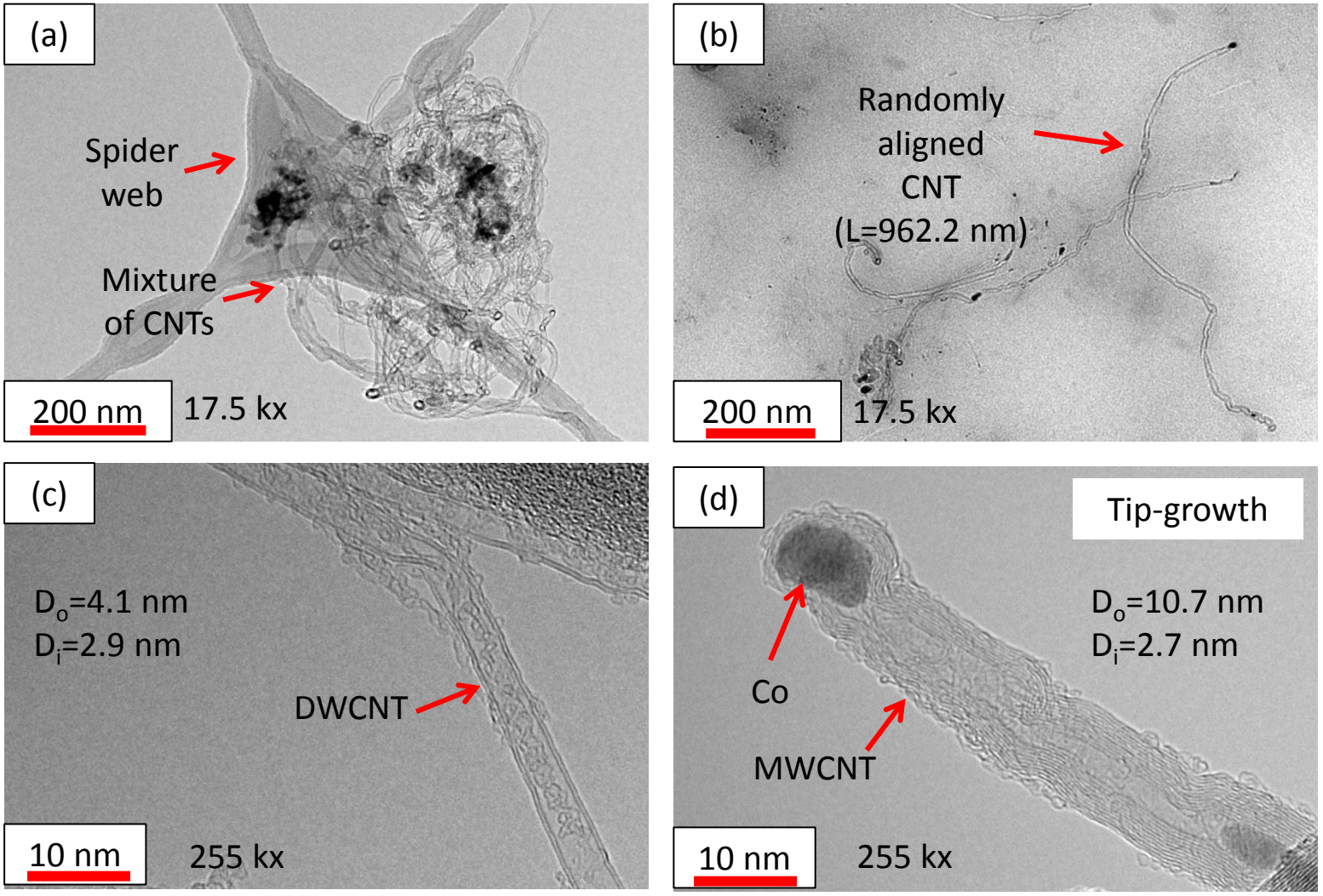

Table 1 I_G/I_D and I_D/I_G ratios of the as-grown CNT grown at various CVD processing temperatures

T_{CVD} (^{0}C)	I_G/I_D Ratio	I_D/I_G Ratio
650	3.94	0.25
675	4.52	0.22
700	6.40	0.16
725	4.09	0.24
750	3.88	0.26